ADVANCED FUNCTIONAL MATERIALS
www.afm-journal.de

Materials Views
www.MaterialsViews.com

Interfacial Reaction-Directed Synthesis of Ce–Mn Binary Oxide Nanotubes and Their Applications in CO Oxidation and Water Treatment

*Guozhu Chen, Federico Rosei, and Dongling Ma**

Interfacial oxidation–reduction reaction is herein developed to prepare hollow binary oxide nanostructures. Ce–Mn nanotubes are fabricated by treating $Ce(OH)CO_3$ templates with $KMnO_4$ aqueous solution, where MnO_4^- is reduced to manganese oxide and the Ce^{3+} in $Ce(OH)CO_3$ is simultaneously oxidized to form cerium oxide, followed by selective wash with HNO_3. The resulting Ce–Mn binary oxide nanotubes exhibit high catalytic activity towards CO oxidation and show significant adsorption capacity of Congo red. Moreover, guided by the same interfacial-reaction principle, binary oxide hollow nanostructures with different shapes and compositions are synthesized. Specifically, hollow Ce–Mn binary oxide cubes, and Co-Mn and Ce-Fe binary oxide hollow nanostructures are achieved by changing the shape of the $Ce(OH)CO_3$ templates from rods to cubes, by changing the tempates from $Ce(OH)CO_3$ nanorods to $Co(CO_3)_{0.35}Cl_{0.20}(OH)_{1.10}$ nanowires, and by replacing the oxidant of $KMnO_4$ with another strong one, K_2FeO_4, respectively. This work is expected to open a new, simple avenue for the general synthesis of hollow binary oxide nanostructures.

1. Introduction

Transition-metal oxide nanotubes represent a promising class of materials due to their potential applications (e.g. catalysis, ferroelectric, lithium storage, and gas sensors).[1–4] Among a wealth of studies on the fabrication of nanotubes, template-assisted synthesis based on interfacial reaction is an effective approach, where the templates are normally designed to chemically react with given reactants following various pathways, such as ion exchange[5–7] and Kirkendall diffusion,[8–10] and the residual templates often need to be removed later on. Therefore, in this approach the selection of appropriate templates is critical not only for the formation of hollow structures, but also for their chemical purity. To be more specific, the templates should be easily removed by either washing or calcination without causing the collapse of the shell. So far, most nanotubes synthesized by this approach are single metal oxides despite the increasing interest in binary metal oxides, which exhibit remarkable improvement of properties (e.g., gas sensing) compared to corresponding single components.[11–17] It is thus worthwhile to extend this interfacial reaction-based approach further to the preparation of binary metal oxide nanotubes. Such exploration can add a new, simple avenue for the general synthesis of binary oxide nanotubes in addition to currently used methods (e.g., electrospinninng[16] and anodization[17]).

Ce–Mn binary oxides, as environmentally friendly catalysts, have been extensively studied in many reactions, such as CO oxidation, selective catalytic reduction of NO_x with NH_3, and oxidation of volatile organic compounds.[18–22] Until now, typically there are three routes, namely, precipitation, impregnation and sol-gel methods to synthesize the Ce–Mn binary oxide nanoparticles. Besides the consistently irregular morphology of Ce–Mn binary oxide nanoparticles achieved from these methods, high temperature (400~800 °C) calcination is a necessary step in these routes. Therefore, both simplifying synthesis strategies and controlling the morphology of the Ce–Mn binary oxide are areas of interest for further enhancing their widespread applications.

In previous work, we chose $Ce(OH)CO_3$ nanorods as template and successfully fabricated CeO_2 nanotubes and $CePO_4$:Tb nanotubes through different interfacial reactions.[23–25] Thanks to the unique feature of $Ce(OH)CO_3$, the template can be easily removed by acid wash or calcination. Moreover, the outward diffusion of Ce^{3+} ions in the template is faster than the inward diffusion of OH^- ions from solution during the reaction of Ce^{3+} with NaOH solution, which is responsible for the formation of Kirkendall-type voids in the CeO_2 nanotubes. Last but not least, the solubility product constants of $Ce(OH)_3$ and $CePO_4$ are smaller than that of $Ce(OH)CO_3$, which is a key factor for transforming $Ce(OH)CO_3$ into CeO_2 and $CePO_4$. It should be noted that there are no valence changes (i.e. no oxidation–reduction reactions are involved) for the participating species in these specific interfacial reactions. Considering the reduction ability of Ce (III), these highly interesting $Ce(OH)CO_3$ nanorod templates may be further employed in the interfacial oxidation–reduction reactions with oxidizing agents to form binary oxide nanotubes. As a matter of fact, the interfacial oxidation–reduction

Dr. G. Chen, Prof. F. Rosei, Prof. D. Ma
Institut National de la Recherche Scientifique
1650 Boulevard Lionel Boulet
Varennes, Québec, J3X 1S2, Canada
E-mail: ma@emt.inrs.ca

DOI: 10.1002/adfm.201200900

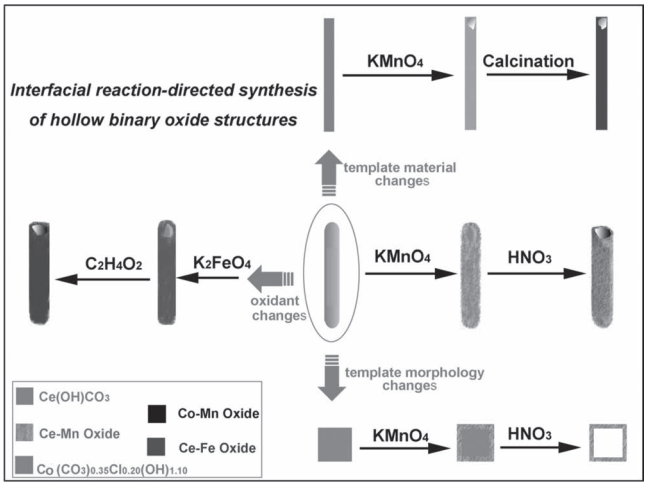

Scheme 1. Schematic illustration of the facile synthesis of hollow binary oxide nanostructures.

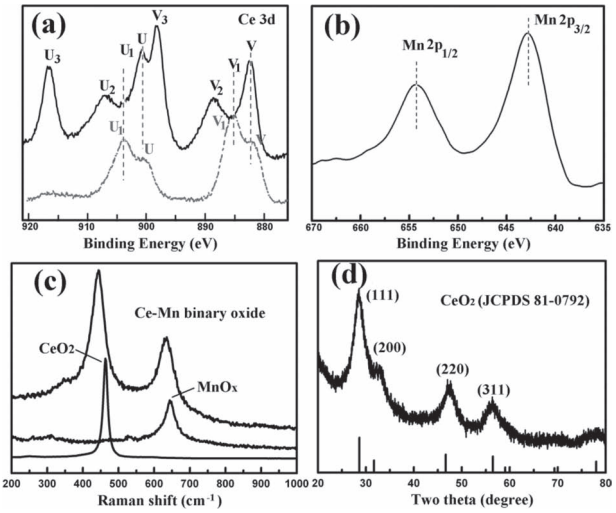

Figure 1. XPS spectra of Ce 3d of the as-prepared sample (solid black line) and $Ce(OH)CO_3$ nanorod templates (dotted gray line) (a); Mn 2p of the as-prepared sample (b); Raman spectra of the as-prepared sample, and commercial CeO_2 and MnO_2 particles (c) and XRD pattern of the sample after heat treatment at 200 °C (d).

reaction has recently been explored for the synthesis of hollow structures or binary oxides.[26–28] For example, hollow MnO_2 structures were prepared by the interfacial reaction between $KMnO_4$ and $MnCO_3$ oxidation–reduction pairs, followed by the removal of unreacted $MnCO_3$.[27] Co_3O_4@MnO_2 core@shell arrays were also synthesized under the guidance of the interfacial oxidation–reduction reaction,[28] where the authors deposited a carbon layer on pre-synthesized Co_3O_4 nanowires as templates, followed by oxidation–reduction between the deposited carbon layer and $KMnO_4$. The introduction of the carbon layer is crucial to the oxidation–reduction reaction; without carbon, no MnO_2 can be observed on the Co_3O_4 nanowire surface. In both examples introduced above, $KMnO_4$ is reduced to MnO_2, either by $MnCO_3$ or by C. Taking both the strong oxidation ability of $KMnO_4$ and reduction ability of Ce(III) into account, it is expected that Ce–Mn binary oxide nanotubes can be synthesized by the interfacial oxidation–reduction reaction between $KMnO_4$ and $Ce(OH)CO_3$ nanorods under certain conditions.

In this paper, we report the simple and robust preparation of Ce–Mn binary oxide nanotubes by employing $Ce(OH)CO_3$ nanorods as templates, which directly react with $KMnO_4$ aqueous solution and do not require any additional "intermediate" layers (such as carbon) to finish the oxidation–reduction reaction. The resulting Ce–Mn binary oxide nanotubes exhibit high catalytic activity towards CO oxidation and exhibit significant adsorption capacity of Congo red. Moreover, guided by the same interfacial-reaction principle, hollow Ce–Mn binary oxide cubes are also achieved by utilizing $Ce(OH)CO_3$ cubes as templates. Although the focus herein is on the Ce–Mn binary oxide, we also demonstrate that this method can be easily extended to fabricate other hollow binary oxide nanocomposites, such as Co-Mn and Ce-Fe binary oxides, when suitable templates and oxidation/reduction pairs are chosen (**Scheme 1**).

2. Results and Discussion

X-ray photoelectron spectroscopy (XPS) was first used to examine the valence states of Ce and Mn after the interfacial reaction. As shown in **Figure 1**a, the as-prepared sample (the solid black line) and $Ce(OH)CO_3$ nanorods (dotted gray line) show quite different Ce 3d XPS patterns. Four peaks U, U_1, V and V_1, characteristic of Ce(III), are clearly present in the $Ce(OH)CO_3$ nanorods, while six peaks labeled U, U_2, U_3, V, V_2, and V_3, characteristic of Ce(IV),[29] are observed in the as-prepared sample, indicating the oxidation of Ce(III) during the interfacial reaction. In the case of Mn 2p spectrum, an intense peak of Mn $2p_{3/2}$ around 643 eV suggests that Mn(IV) is dominant Mn-species in the as-prepared sample (Figure 1b).[18] The XPS results provide strong evidence that an interfacial oxidation–reduction reaction takes place between the $KMnO_4$ and $Ce(OH)CO_3$ nanorods. This was further confirmed by Raman spectroscopy measurements (Figure 1c), where two peaks are clearly present in the Raman spectrum of the as-prepared sample. The peak centered at ~458 cm^{-1} is due to the symmetric breathing mode of oxygen atoms around cerium ions in the cubic-phase cerium oxide, while the other peak centered at 633 cm^{-1} is characteristic of the Mn-O stretching mode of manganese oxides.[30] The co-existence of Ce and Mn in the as-preapred sample was also supported by Energy Dispersive Spectroscopy (EDS) measurements, which yields the stoichiometry value of Ce:Mn ≅ 0.4:0.6 (Figure S1). X-ray Diffraction (XRD) characterization was conducted to study the crystalline structure of the Ce–Mn binary oxide. Only a very weak, broad peak was observed in the as-prepared sample (Figure S2), denoting the lack of any significant "long-range" crystalline order. The remarkable increase of diffraction peaks is clearly visible after treating the sample at an elevated temperature of 200 °C for 2 h. No characteristic diffraction peaks of manganese oxides and $Ce(OH)CO_3$ nanorods are present and all diffraction peaks can be well indexed to CeO_2 (JCPDS81-0792). This is consistent with previous reports concerning the structure features of MnO_x-CeO_2 binary oxide.[18–20] All these results consistently demonstrate that the Ce–Mn binary oxide is formed via the

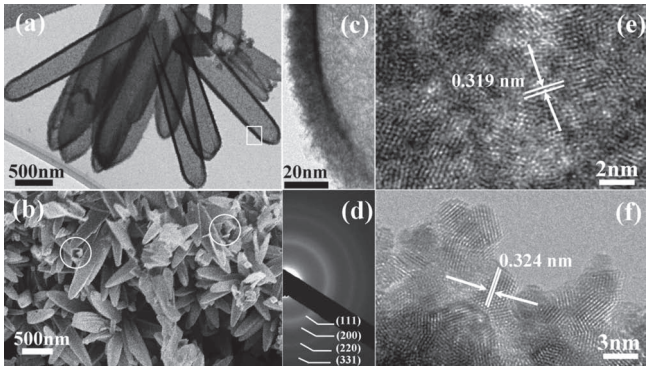

Figure 2. TEM (a) and SEM (b) images of the prepared Ce–Mn binary oxide nanotubes without heat treatment; (c) magnified TEM image of the rectangle part in (a); SAED pattern (d); HRTEM images of the inner surface (e) and the outer surface (f) of the heat-treated nanotubes.

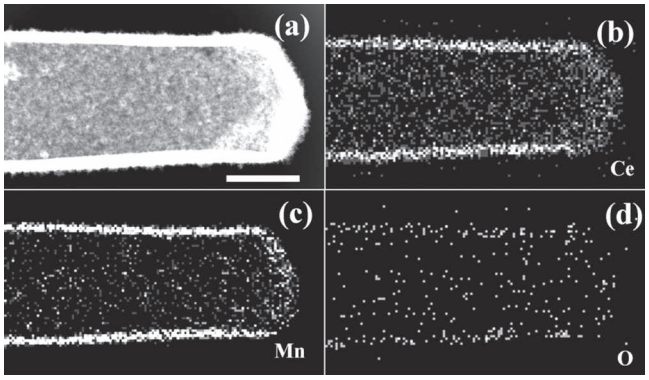

Figure 3. HAADF-STEM image (a), and Ce-L (b), Mn-K (c) and O-K (d) STEM-EDX maps of an individual nanotube after heat treatment. Scale bar: 200 nm.

interfacial oxidation–reduction reaction between $KMnO_4$ and $Ce(OH)CO_3$ nanorods.

The morphology and size of the Ce–Mn binary oxide were evaluated by transmission electron microscopy (TEM) and scanning electron microscopy (SEM). The sharp contrast between the edge and center parts of these one-dimensional structures is characteristic of a nanotube morphology (**Figure 2**a). The as-prepared nanotubes inherit the shape and dimensions of the $Ce(OH)CO_3$ nanorod template (Figure S3). Most of the nanotubes have diameters of 300–350 nm, with typical wall thickness of around 40 nm. Figure 2b presents a typical SEM image of the Ce–Mn binary oxide nanotubes, where some open nanotubes can be identified (indicated by circles). As shown in Figure 2c, the as-prepared nanotube reveals a rather rough surface morphology with fluff-like nanostructures, which is in clear contrast to the smooth surface of the $Ce(OH)CO_3$ template. These "fluffs" are loosely connected, similar to those of hollow MnO_2 and Co_3O_4@MnO_2 core@shell nanowires prepared from reduction-oxidation interfacial reactions, where the "fluffs" were indexed to MnO_2.[27,28] In our work, the EDS analysis focusing on the "fluff" exhibits the coexistence of Mn and Ce elements. However, due to the low crystallinity of the "fluff", it is difficult to characterize their structure in detail from either high Resolution TEM (HRTEM) image or Selected Area Electron Diffraction (SAED) (Figure S4). Nonetheless, after a slight heat treatment at 200 °C for 2 h, high-intensity diffraction rings appear in the SAED with the entire pattern well indexed to a cubic phase of CeO_2 (Figure 2d). HRTEM characterization reveals that the surface morphology of the nanotubes also changes after such heat treatment. The "fluffs" disappear and both the inner and outer walls of the nanotubes are mainly composed of small nanoparticles (Figure 2e, f). Most of them are 2–3 nm in dimensions and highly crystalline, randomly oriented with each other. The interlayer spacing is measured to be ~0.32 nm, which could be indexed well to the {111} crystal planes of the cubic CeO_2 structure. Since catalytic performance highly depends on the structure stability of catalysts that is normally enhanced with crystallization, catalytic properties were only studied for the heat-treated samples.

To further investigate the elemental distribution of Ce and Mn in the nanotubes, scanning transmission electron microscopy (STEM)–energy-dispersive X-ray (EDX) line scans were conducted on an individual nanotube (Figure S5). Both Ce and Mn show bimodal distributions with their maxima located in the edge part, while their minima in the center. Corresponding high angle annular Dark field (HAADF)-STEM image and elemental maps are shown in **Figure 3**. We observe that Ce, Mn and O are uniformly distributed in the wall of this representative nanotube. Such uniform distribution of Ce and Mn is beneficial to strengthen the interaction between Ce and Mn, if any, in the binary oxide.[27]

When the $Ce(OH)CO_3$ nanorods are mixed with $KMnO_4$ aqueous solution, there is a liquid-solid interface reaction between the $Ce(OH)CO_3$ nanorods and MnO_4^-. Therefore, the $Ce(OH)CO_3$ nanorods not only act as templates but also participate in the chemical reaction for the synthesis of binary oxide nanotubes. At an initial stage, MnO_4^- can quickly oxidize Ce(III) on the $Ce(OH)CO_3$ template surface, as reflected from the color change of $Ce(OH)CO_3$ from white to light brown within 10 minutes. When the reaction time is shorter than 3 days, the thickness of the wall is too thin to keep the tube structure stable during the process removing residual $Ce(OH)CO_3$ with acid (**Figure 4**a, b). As the reaction prolongs, the wall becomes thicker and thicker, and thus perfect nanotubes can be maintained after acid treatment (Figure 4c, d). Some segmented voids (**Figure 5**a, b) appear in the $Ce(OH)CO_3$ nanorods after 9 days of the interfacial reaction even before acid washing, which is similar to that shown in our previous report where the so-called Kirkendall-diffusion is responsible for the formation of CeO_2 nanotubes.[25]

Both the formation of the uniformly distributed cerium and manganese oxides and the segmented voids can be explained as follows. In the herein discussed $Ce(OH)CO_3$-$KMnO_4$ system, once MnO_4^- ions oxidize Ce^{3+} ions slowly dissociated from the $Ce(OH)CO_3$ nanorods (equation 1), MnO_4^- is reduced to manganese oxide (equation 2), and the Ce^{3+} is simultaneously oxidized to form CeO_2 (equations 3 and 4). Both types of oxide particles are nucleated and synthesized at ultra-small sizes and are in close contact with each other, forming an intimate mixture. The whole process is similar to the redox-precipitation reaction reported by Arena et al.[21] In that scenario, MnO_4^- ions were mixed with Ce^{3+} and Mn^{2+} ions in a basic solution (pH~8) to

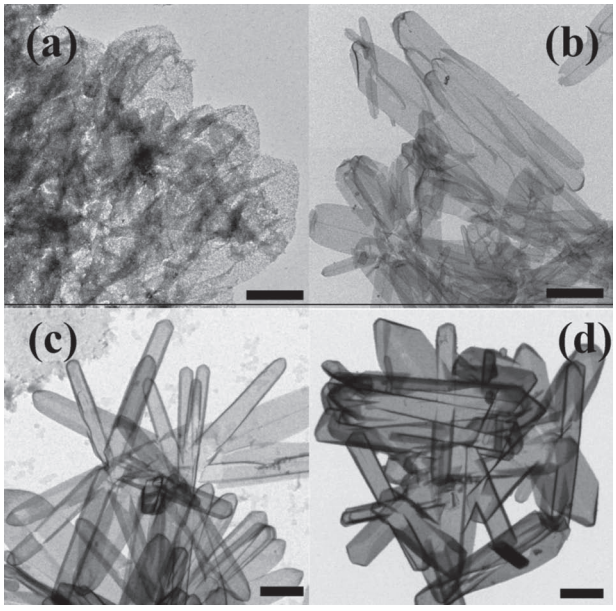

Figure 4. TEM images of the as-prepared Ce–Mn binary oxide products after different reaction time: (a) 1, (b) 3, (c) 4, and (d) 6 days without heat treatment. Scale bar: 500 nm.

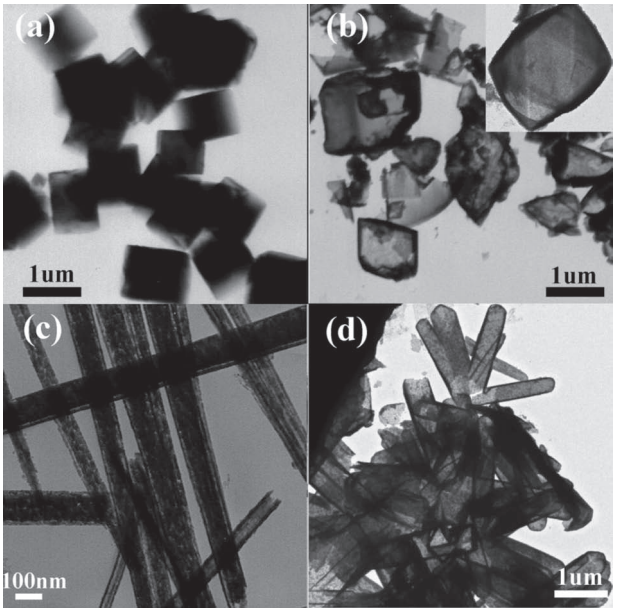

Figure 6. TEM images of (a) $Ce(OH)CO_3$ cube templates and (b) as-prepared hollow Ce–Mn binary oxide cubes without further heat-treatment. (c) Co-Mn binary oxide and (d) Ce-Fe binary oxide hollow structures. Inset in (b) is a magnified hollow cube.

attain a mixture of MnO_2 and CeO_2 species at the atomic level. In our case, although the pH value of the initial reaction solution was set at ~7, it gradually increased to ~9 after reaction due to the release of OH^- ions from the slow dissociation of the $Ce(OH)CO_3$ nanorods (equation 1) and the reduction reaction of the MnO_4^- ions (equation 2). The newly formed oxides cover the surface, preventing a direct chemical reaction between MnO_4^- in solution and Ce^{3+} in the $Ce(OH)CO_3$ nanorods. Further reaction relies on the diffusion of Ce^{3+} and/or MnO_4^- through the outer wall. Due to the different ionic radii of Ce^{3+} and MnO_4^-, the outward diffusion of Ce^{3+} in the $Ce(OH)CO_3$ nanorods is faster than the inward diffusion of MnO_4^- from solution.[10] A net outflow of Ce^{3+} ions through the outer wall results in the opposite transport of lattice vacancies and eventually the formation of the segmented voids.

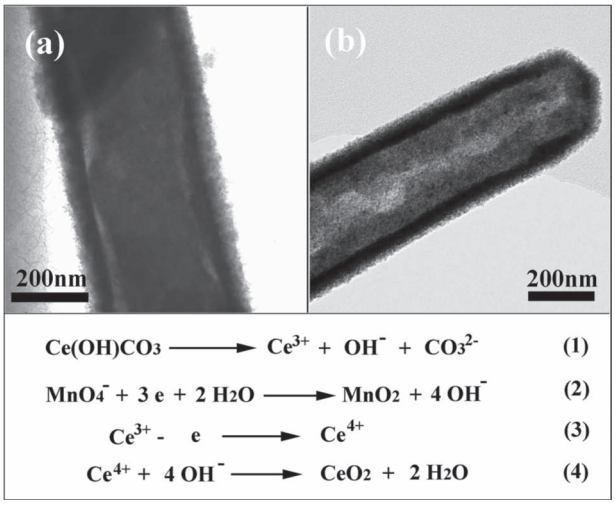

Figure 5. TEM images of typical nanorods with segmented voids without acid and heat treatments and relevant chemical equations.

We anticipate that this method can be extended to prepare hollow structures with different shapes and compositions, provided suitable templates and oxidants can be identified. For example, hollow Ce–Mn cubes can be obtained when solid $Ce(OH)CO_3$ cubes are used as template (**Figure 6**a,b). When $Ce(OH)CO_3$ nanorod templates are replaced by $Co(CO_3)_{0.35}Cl_{0.20}(OH)_{1.10}$ nanowires, the Co (II) in the $Co(CO_3)_{0.35}Cl_{0.20}(OH)_{1.10}$ is expected to be oxidized by $KMnO_4$ since Co has variable valency. As shown in Figure S6, after 6 days of the interfacial reaction between $Co(CO_3)_{0.35}Cl_{0.20}(OH)_{1.10}$ and $KMnO_4$ at room temperature, hollow structures are clearly observed in the TEM image. As mentioned in the paper, the Kirkendall diffusion is responsible for the initial formation of the hollow structure owing to the outward diffusion of Co^{2+} in the $Co(CO_3)_{0.35}Cl_{0.20}(OH)_{1.10}$ nanowires is faster than inward diffusion of MnO_4^- ions from solution. Once calcined for decomposition of the residual $Co(CO_3)_{0.35}Cl_{0.20}(OH)_{1.10}$, the sample is transformed into porous Co-Mn binary oxide nanotubes (Figure 6c). The voids aroused by the Kirkendall diffusion and the vacancies resulted from gas release during the calcinations process are possibly responsible for the final porous structures. Another example is the generation of Ce-Fe binary oxide nanotubes when K_2FeO_4 (a strong oxidizing agent) is engaged to react with the $Ce(OH)CO_3$ nanorods (Figure 6d). FeO_4^{2-} ions are reduced to Fe^{3+} ions, which are easily hydrolyzed in solution to form $Fe(OH)_3$. The dehydration of $Fe(OH)_3$ during subsequent heat treating process (drying) results in the formation of iron oxide. The Ce^{3+} is oxidized to form CeO_2 simultaneously, as discussed above.

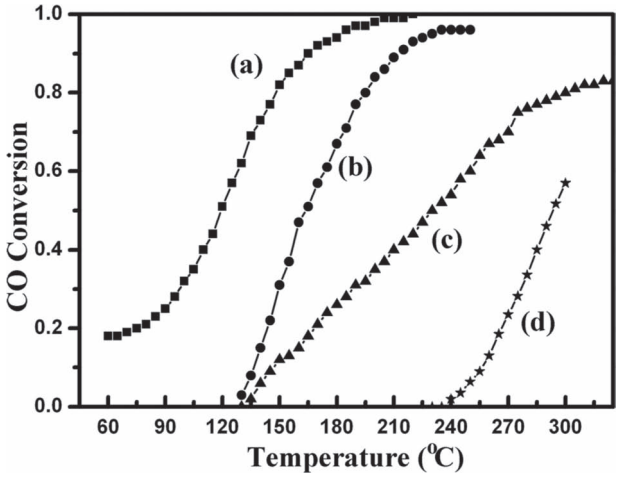

Figure 7. CO conversion as a function of temperature for (a) Ce–Mn binary oxide nanotubes; (b) MnO_2; (c) physical mixture of MnO_2 and CeO_2 and (d) CeO_2.

As aforementioned, Ce–Mn binary oxide nanoparticles are being used in many catalytic reactions. Due to the intimate and synergistic interaction between manganese and cerium oxide, Ce–Mn binary oxide nanoparticles usually exhibit higher catalytic activity than single components. Herein, we study the catalytic activity of Ce–Mn binary oxide nanotubes and compare it with that of commercially available MnO_2 and CeO_2 particles and their physical mixture using CO oxidation as a model reaction. Their light-off curves for CO oxidation are presented in **Figure 7**. The activity follows the order of Ce–Mn binary oxide nanotubes > MnO_2 > physical mixture of MnO_2 and CeO_2 > CeO_2. Specifically, 50% CO conversion is realized at 120 °C with the presence of the Ce–Mn binary oxide nanotubes, in clear contrast to 165 °C with MnO_2, 295 °C with CeO_2 and 235 °C with the physical mixture of MnO_2 and CeO_2 particles. In comparison with pure CeO_2 or MnO_2 particles, Ce and Mn in the Ce–Mn binary oxide nanotubes interact with each other and contribute to CO oxidation synergistically. Specifically, the active sites of MnO_2 provide oxygen species because of the multiple valence state of Mn, while CeO_2, as an oxygen reservoir, stores and releases oxygen via the redox shift between Ce^{4+} and Ce^{3+} under oxidizing and reducing conditions, respectively.[31] Therefore, oxygen atoms transfer from O_2 to the active sites of MnO_2 through the oxygen reservoir of CeO_2 that is in close contact with MnO_2, greatly increasing oxygen mobility on the Ce–Mn binary oxide surface and realizing effective activation of molecular oxygen in the CO oxidation process.[18] The extremely uniform and high dispersion of active components throughout the nanotube wall and thereby the intimate and strong interaction between Ce and Mn, however, are highly likely responsible for the much higher catalytic activity of the nanotubes as compared with the physical mixture, where the Ce–Mn interaction is supposed to be insignificant among separate, large sized CeO_2 and MnO_2 particles. In addition, the ultra-small crystallite size of the nanoparticles in the nanotubes and the hollow structure together lead to a high specific surface area (~202 m^2/g), which definitely also contributes to the better performance of the nanotubes. Last but not least, the hollow structure enables the better contact of catalytically active particles with the gas molecules due to the existence of the interior space and penetrable wall, which is also beneficial for gas-phase reactions.

In addition, hollow structures with high surface area have also emerged as an attractive platform for water treatment (e.g. the removal of Congo red).[27,32] The binary oxide nanotubes developed herein are found to exhibit significant adsorption capacity of Congo red (**Figure 8**). The estimated adsorption capacity of Congo red at 10 min is about 100 mg g^{-1} for Ce–Mn binary oxide nanotubes, 24 mg g^{-1} for CeO_2 nanotubes, 21 mg g^{-1} for commercial MnO_2 and 7 mg g^{-1} for commercial CeO_2. It is interesting to note that the CeO_2 nanotubes with the similar cavity prepared from the same $Ce(OH)CO_3$ template,[23] exhibit considerably inferior adsorption performance in comparison to Ce–Mn binary oxide nanotubes. Brunauer-Emmett-Teller (BET) measurements show that the specific surface area of the Ce–Mn binary oxide nanotubes (inset in Figure b) is far higher than that of the CeO_2 nanotubes (~74 m^2/g) even though they have the similar tubular structures. The higher surface area of Ce–Mn binary oxide nanotubes might be ascribed to smaller crystallite size (~2 nm) and much rougher surface in comparison to that of CeO_2 nanotubes (crystallite size, ~6 nm).[23]

3. Conclusions

In summary, Ce–Mn binary oxide nanotubes were successfully fabricated by easily reacting the $Ce(OH)CO_3$ nanorods with $KMnO_4$ aqueous solution, followed by selective wash with HNO_3. Since the reaction can be carried out at mild conditions,

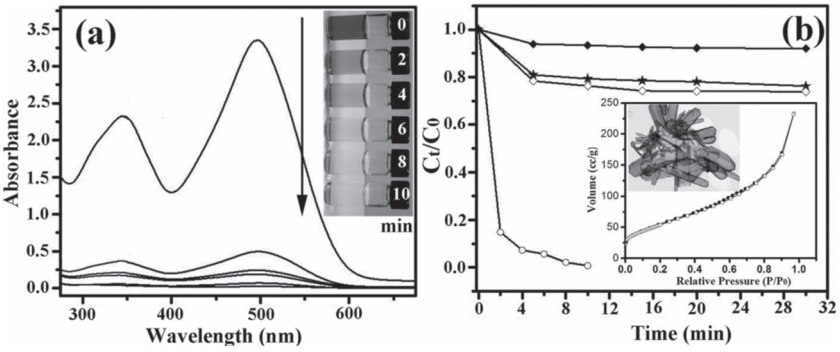

Figure 8. a) absorption spectra of a solution of Congo red (100 mg/L, 20 mL) in the presence of Ce–Mn binary oxide nanotubes (20 mg) at different time intervals (min). Insets in (a) are corresponding photographs of Congo red with time. (b) Adsorption rate of the Congo red on: commercial CeO_2 (denoted as "solid square"); MnO_2 (stars); CeO_2 nanotubes (blank square), and Ce–Mn binary oxide nanotubes (blank circle). C_0 (mg/L) is the initial concentration of the Congo red in solution and C (mg/L) is the concentration of the Congo red at different adsorption time. Inset in (b) is the nitrogen adsorption-desorption isotherms of Ce–Mn binary oxide nanotubes.

it should be straightforward to scale up the entire process for high-volume production of the Ce–Mn binary oxide nanotubes. Due to the strong interaction between CeO_2 and MnO_2 in the Ce–Mn binary oxide and the high specific surface area, the Ce–Mn binary oxide nanotubes exhibit high catalytic activity towards CO oxidation in comparison with both commercially available CeO_2 and MnO_2 particles and their physical mixture. In addition, the nanotubes display excellent adsorption performance when used to remove a common organic waste of Congo red from water, suggesting their potential application in water treatment. This work also represents the first demonstration of an interfacial oxidation–reduction reaction-engaged process capable of generating binary oxide hollow nanostructures with different shapes and compositions from the solution phase.

4. Experimental Section

Materials: Cerium (III) nitrate hexahydrate ($Ce(NO_3)_3{\cdot}6H_2O$), cobalt(II) chloride hexahydrate ($CoCl_2{\cdot}6H_2O$), urea (NH_2CONH_2), potassium permanganate ($KMnO_4$), potassium ferrate (K_2FeO_4), sodium hydroxide (NaOH), nitric acid (HNO_3) and acetic acid ($C_2H_4O_2$) were purchased from Sigma-Aldrich and used without further purification. Water was purified by a Millipore Ultrapure water system and has a resistivity of 18.2 MΩ·cm at 25 °C.

Synthesis of $Ce(OH)CO_3$ templates: In a typical experiment, $Ce(NO_3)_3{\cdot}6H_2O$ (4 mmol) and urea (24 mmol) were added to water (80 mL) under vigorous magnetic stirring at 80 °C for 24 h. The obtained powder sample was centrifuged, washed with distilled water and dried.[23]

Synthesis of $Ce(OH)CO_3$ cube-like templates and $Co(CO_3)_{0.35}Cl_{0.20}(OH)_{1.10}$ nanowire templates: These two types of templates were synthesized by simple hydrothermal methods. For $Ce(OH)CO_3$ cube-like templates, $Ce(NO_3)_3{\cdot}6H_2O$ (0.05 M) solution and $CO(NH_2)_2$ (0.1 M) solution were mixed, then hydrothermally reacted at 160 °C for 1 h;[33] In the case of $Co(CO_3)_{0.35}Cl_{0.20}(OH)_{1.10}$ nanowires, $CoCl_2{\cdot}6H_2O$ (5 mmol) and $CO(NH_2)_2$ (5 mmol) were dissolved in 40 ml of water and heated at 100 °C for 12 h.[34]

Synthesis of Ce–Mn Binary Oxide Nanotubes: $Ce(OH)CO_3$ powder (5 g) was mixed with $KMnO_4$ (60 ml, 0.025 M) aqueous solution. After stirring 10min, the mixture was kept still for 6 days. Finally, the sample was removed and washed by HNO_3 (1M) thoroughly to remove unreacted templates, and dried at 60 °C.

Synthesis of Hollow Ce–Mn Cubes and Co-Mn, Ce-Fe Composites: For the preparation of Ce–Mn binary oxide nanocubes, $Ce(OH)CO_3$ nanocubes (50 mg) were mixed with $KMnO_4$ (30 ml, 0.5 mM) aqueous solution. After stirring 10 min, the mixture was kept still for 6 days. Finally, the sample was washed by HNO_3 (1 M) thoroughly to remove unreacted templates, and dried at 60 °C. While for the preparation of hollow Co-Mn, $Co(CO_3)_{0.35}Cl_{0.20}(OH)_{1.10}$ (50 mg) was dispersed in water (30 ml), followed by the addition of $KMnO_4$ (2.5 ml, 0.05 M). Then, the mixture was kept still for 9 days before washing by water thoroughly. Finally, the sample was calcined at 350 °C for 4 h. For the preparation of hollow Ce-Fe, $Ce(OH)CO_3$ powder (300 mg) was mixed with K_2FeO_4 (30 ml, 0.025 M) aqueous solution. After stirring 10 min, the mixture was kept still for 6 days. Finally, the sample was washed, and then washed by acetic acid thoroughly to remove unreacted templates, and dried at 60 °C.

Materials Characterization: The samples were characterized by powder XRD (Bruker D-8 Advance) with Cu-kα radiation, SEM (6700F), TEM (JEM-2100) equipped with an EDS. Micro-Raman measurements were taken with an RM 1000 Renishaw Raman microscope system equipped with a laser at 514 nm, a Leica microscope and an electrically refrigerated CCD camera. Brunauer-Emmet-Teller surface area measurements were performed for the catalysts with a Quantachrome Instruments Autosorb-1. UV-vis adsorption spectra were measured on a Cary 5000 UV-Vis-NIR spectrophotometer (Varian). XPS spectra were taken using a VG Escalab 220i-XL equipped with a twin anode X-ray source.

CO Oxidation: Catalytic activity was measured using a continuous flow fixed-bed microreactor at atmospheric pressure. In a typical experiment, the system was first purged with high-purity N_2 gas and then a gas mixture of $CO/O_2/N_2$ (1:10:89) was introduced into the reactor which contained 50 mg of the Ce–Mn binary oxide nanotubes. Gases were analyzed with an online infrared gas analyzer (Gasboard-3121, China Wuhan Cubic Co.) which simultaneously detects CO and CO_2 with a resolution of 10 ppm. The results were further confirmed with a Shimadzu gas chromatograph (GC-14C). For the purpose of comparison, the CO oxidation tests were also run on commerical MnO_2 and CeO_2 particles, as well as their physical mixture under exactly same conditions. MnO_2 particles (mean size ~10 μm) and CeO_2 particles (mean size ~0.5 μm) were ordered from Sigma-Aldrich and used without further purification.

Water Treatment Experiment: The adsorbent sample (20 mg) was added to Congo red (Sigma-Aldrich, 99%) solution (20 ml, 100 mg/L) under stirring. UV-Vis absorption spectra were recorded at different intervals to monitor the process. CeO_2 nanotubes were prepared according to our previously reported procedures.

Supporting Information

Supporting Information is available from the Wiley Online Library or from the author.

Acknowledgements

Financial support from the Natural Sciences and Engineering Research Council of Canada (NSERC) through a Strategic Grant and Discovery Grants, and from Agence de l'efficacité énergétique is greatly appreciated.

Received: March 29, 2012
Published online: May 25, 2012

[1] L. M. Sanchez-Amaya, M. Lopez-Haro, E. Rio, A. B. Hungria, P. Midgley, J. J. Calvino, S. Bernal, F. J. Botana, *Nano Lett.* **2009**, *9*, 1395.
[2] Y. Wang, H. C. Zeng, J. Y. Lee, *Adv. Mater.* **2006**, *18*, 645.
[3] C. Yan, L. Nikolova, A. Dadvand, C. Harnagea, A. Sarkissian, D. F. Perepichka, D. Xue, F. Rosei, *Adv. Mater.* **2010**, *22*, 1741.
[4] J. Chen, L. Xu, W. Li, X. Gou, *Adv. Mater.* **2005**, *17*, 582.
[5] X. W. Lou, L. A. Archer, Z. Yang, *Adv. Mater.* **2008**, *20*, 3987.
[6] X. Jiang, B. Mayers, T. Herricks, Y. Xia, *Adv. Mater.* **2003**, *15*, 1740.
[7] W. Cho, Y. H. Lee, H. J. Lee, M. Oh, *Adv. Mater.* **2011**, *23*, 1720.
[8] H. J. Fan, U. Gösele, M. Zacharias, *Small* **2007**, *3*, 1660.
[9] Y. Zhu, W. Chen, C. Nan, Q. Peng, R. Wang, Y. Li, *Cryst. Growth Des.* **2011**, *11*, 4406.
[10] Y. Yin, R. Rioux, C. Erdonmez, S. Hughes, G. Somorjai, A. Alivisatos, *Science* **2004**, *304*, 711.
[11] D. F. Zhang, L. D. Sun, C. J. Jia, Z. G. Yan, L. P. You, C. H. Yan, *J. Am. Chem. Soc.* **2005**, 127, 13492.
[12] R. Nechache, C. V. Cojocaru, C. Harnagea, C. Nauenheim, M. Nicklaus, A. Ruediger, F. Rosei, A. Pignolet, *Adv. Mater.* **2011**, *23*, 1724.
[13] H. Tan, J. M. Xue, B. Shuter, X. Li, J. Wang. *Adv Funct Mater.* **2010**, *20*, 722.
[14] W. Zhou, C. Cheng, J. Liu, Y. Y. Tay, J. Jiang, X. Jia, J. Zhang, H. Gong, H. H. Hng, T. Yu, H. J. Fan, *Adv. Funct. Mater.* **2011**, *21*, 2439.
[15] E. Fabbri, L. Bi, D. Pergolesi, E. Traversa, *Adv. Mater.* **2012**, *24*, 195.

[16] L. Xu, H. Song, B. Dong, Y. Wang, J. Chen, X. Bai, *Inorg. Chem.* **2010**, *49*, 10590.
[17] W. Zhang, Z. Xi, G. Li, Q. Wang, H. Tang, Y. Liu, Y. Zhao, L. Jiang, *Small*, **2009**, *5*, 1742.
[18] Z.-Q. Zou, M. Meng, Y.-Q. Zha, *J. Phys. Chem. C* **2010**, *114*, 468.
[19] G. Qi, R. T. Yang, *J. Phys. Chem. B* **2004**, *108*, 15738.
[20] Y. Chen, H. Zheng, Z. Guo, C. Zhou, Z. Wang, A. Borgna, Y. Yang, *J. Catal.* **2011**, *283*, 34.
[21] F. Arena, G. Trunfio, J. Negro, B. Fazio, L. Spadaro, *Chem. Mater.* **2007**, *19*, 2269.
[22] H. Li, G. Qi, Tana, X. Zhang, X. Huang, W. Li, W. Shen, *Appl. Catal. B* **2011**, *103*, 54.
[23] G. Chen, C. Xu, X. Song, W. Zhao, Y. Ding, S. Sun, *Inorg. Chem.* **2008**, *47*, 723.
[24] G. Chen, S. Sun, W. Zhao, S. Xu, T. You, *J. Phys. Chem. C* **2008**, *112*, 20217.
[25] G. Chen, S. Sun, X. Sun, W. Fan, T. You, *Inorg. Chem.* **2009**, *48*, 1334.
[26] B. Li, G. Rong, Y. Xie, L. Huang, C. Feng, *Inorg. Chem.* **2006**, *45*, 6404.
[27] J. Fei, Y. Cui, X. Yan, W. Qi, K. Wang, Q. He, J. Li, *Adv. Mater.* **2008**, *20*, 452.
[28] J. Liu, J. Jiang, C. Cheng, H. Li, J. Zhang, H. Gong, H. J. Fan, *Adv. Mater.* **2011**, *23*, 2076.
[29] L.-S. Zhong, J.-S. Hu, A.-M. Cao, Q. Liu, W.-G. Song, L.-J. Wan, *Chem. Mater.* **2007**, *19*, 1648.
[30] B. Fazio, L. Spadaro, G. Trunfio, J. Negro, F. Arena, *J. Raman Spectrosc.* **2011**, *42*, 1583.
[31] H. Li, G. Qi, Tana, X. Zhang, X. Huang, W. Li, W. Shen, *Appl. Catal. B* **2011**, *103*, 54.
[32] B. Wang, H. Wu, L. Yu, R. Xu, T.-T. Lim, X. W. Lou, *Adv. Mater.* **2012**, *24*, 1111.
[33] H.-C. Wang, C.-H. Lu, *Mater. Res. Bull.* **2002**, *37*, 783.
[34] S. Xiong, J. S. Chen, X. W. Lou, H. C. Zeng, *Adv. Funct. Mater.* **2012**, *22*, 861.